Direct numerical simulation of drag reduction by spanwise oscillating dielectric barrier discharge plasma force

Physics of Fluids ARTICLE scitation.org/journal/phf

Direct numerical simulation of drag reduction by spanwise oscillating dielectric barrier discharge plasma force

Cite as: Phys. Fluids 32, 075101 (2020); doi: 10.1063/5.0007103
Submitted: 19 March 2020 • Accepted: 12 June 2020 •
Published Online: 1 July 2020

A. Altıntaş,[a] L. Davidson, and S.-H. Peng[b]

AFFILIATIONS

Division of Fluid Dynamics, Department of Mechanics and Maritime Sciences, Chalmers University of Technology, SE-412 96 Gothenburg, Sweden

[a]**Author to whom correspondence should be addressed:** altintas@chalmers.se
[b]**Also at:** Swedish Defense Research Agency, FOI, SE-164 90 Stockholm, Sweden.

ABSTRACT

DBD (dielectric barrier discharge) plasma actuators have in recent years become increasingly attractive in studies of flow control due to their light structures and easy implementation, but the design of a series of actuators enabling drag reduction depends on many parameters (e.g., the length of the actuator, the space between actuators, and voltage applied) and remains a significant issue to address. In this study, velocities created by the DBD plasma actuators in stagnant flow obtained by the numerical model are compared with experimental results. Then, a DNS study is carried on, and spanwise oscillated DBD plasma actuators are examined to obtain a drag reduction in a fully developed turbulent channel flow. This study connects the conventional spanwise oscillated force in drag reduction studies with DBD plasma actuators. While the former is one of the most successful applications for the drag reduction, the latter is a most promising tool with its light and feasible structure.

I. INTRODUCTION AND BACKGROUND

It is known that spanwise oscillations can lead to a significant reduction in the skin friction drag and is widely accepted as a promising method for turbulent drag reduction in boundary layers.[1,2] To create a spanwise oscillation, a number of methods are available, such as electromagnetohydrodynamic (EMHD) flow[2] and wall oscillations[3] by which up to 47% reduction in skin friction was reported.[4]

Velkoff and Ketcham used the plasma for active flow control for the first time to manipulate the transition point on a flat plate.[5] Later on, in 1998, a new configuration of electrodes was presented by Roth *et al.*[6] This configuration was able to produce a jet in stagnant air and manipulate the boundary layer of a flat plate. DBD (dielectric barrier discharge) plasma actuators have over recent years attracted increasing attention in studies of drag reduction due to their light structures and easy implementation since the first time used by Roth *et al.*[6,7] A DBD flow-control device usually does not deploy any mechanical components and is often manufactured of very light material.

The DBD-generated body force is two-dimensional, and it has been shown that the wall-normal component of the force is much smaller compared to the component in the plasma-aligned direction.[8] There exists a number of numerical models to mimic plasma discharge. One of the most common numerical methods is the Shyy model, which assumes that the electrohydrodynamic (EHD) force generated by the plasma has a triangular shape on the top of the embedded electrode, which propagates linearly in the wall-normal and spanwise directions.[9]

In several studies, spanwise-applied-force due to DBD plasma actuators has been proved to obtain skin friction drag decrease. Jukes *et al.*[10] and Jukes[11] obtained a drag reduction up to 40% at a friction Reynolds number of 400. Mahfoze and Laizet[12] investigated the drag reduction potential of the streamwise-aligned DBD plasma actuators to produce streamwise-oriented jets, and they reported that it is possible to reduce the drag by about 33%.

It has been shown that the dominant structures of the near-wall region are the streamwise velocity streaks and the quasi-streamwise vortices.[13–15] It has been stated that a turbulence regeneration cycle

exists, which has been claimed does not depend on the outer flow but on the local near-wall region.[14] Furthermore, it has also been claimed that the near-wall streamwise vortices are the single most important turbulent structure to manipulate in order to achieve drag reduction.[16] This is also supported by the observation that streamwise vortices are responsible for both *ejection* and *sweep* events of the bursting process.[17] During the bursting event, approximately 70% of total turbulence production occurs. Thus, weakening or modifying the streamwise vortices is a general approach in near-wall turbulence control studies. However, recent studies have shown that manipulating the near-wall cycle and the corresponding quasi-streamwise vortices is efficient only for low Reynolds numbers.[18,19]

Many studies have addressed the existence of large-scale (LS) and very-large-scale motions that are very important for wall turbulence at high Reynolds numbers.[20–22] Jiménez[20] reported the existence of large eddies with streamwise lengths of the order of 10–20 boundary-layer thicknesses in the logarithmic region of wall-bounded flows. These large eddies involve mostly streamwise velocity fluctuations and contain most of the streamwise kinetic energy. Many subsequent studies have reported that log-law LS motions strongly influence near-wall turbulent structures.[23–28] In a recent study, Altıntaş *et al.*[29] showed the effect of the LS motions on the near-wall turbulence in a frictional Reynolds number of 550.

This study aims to obtain a skin friction drag reduction by means of spanwise oscillated body force generated by DBD plasma actuators in a turbulent channel flow. The body force is created by a series of spanwise aligned plasma areas that mimics DBD plasma actuators. The force created in this numerical study could be generated by sinusoidal shape embedded electrodes experimentally.[30] A drag reduction is obtained in the present study with the plasma-generated body force oscillating in the spanwise direction. We also analyze the results to explore in which way the turbulent structures have been manipulated or modified. Direct numerical simulations are performed for a turbulent channel flow. The study has been performed with a frictional Reynolds number of $Re_\tau = 180$, and the forcing method is also evaluated for a higher Reynolds numbers of $Re_\tau = 550$.

The paper is organized as follows: The numerical method followed by the derivation and validation of the body force is given in Sec. II. In Sec. III, the results are presented and discussed, and some concluding remarks are given in Sec. IV.

II. SIMULATION METHODOLOGIES

A. Direct numerical simulations

The governing equations to solve in DNS for an incompressible Newtonian fluid are

$$\frac{\partial \mathbf{u}}{\partial t} + \mathbf{u}\cdot\nabla\mathbf{u} = \hat{\mathbf{e}_1}\cdot\tilde{\mathbf{I}} - \frac{1}{\rho}\nabla p + \nu\nabla^2\mathbf{u} + F_z, \tag{1}$$

$$\nabla\cdot\mathbf{u} = 0, \tag{2}$$

where a spanwise directed volume force, F_z, is added as a body force to the Navier–Stokes equations. Here, $\mathbf{u}$, p, ρ, and ν are the velocity vector, the pressure, the fluid density, and the molecular kinematic viscosity of the fluid, respectively. The first term on the right-hand side of Eq. (1) is the prescribed driving pressure gradient.

An implicit, two-step time-advancement finite volume method is used.[31] The central differencing scheme is used in space, and the Crank–Nicolson scheme is used in the time domain. The Navier–Stokes equation for u_i, Eq. (1), in discretized form can be written as

$$u_i^{n+1} = u_i^n + \Delta t H\left(u_i^n, u_i^{n+1}\right) - \frac{1}{\rho}\alpha\Delta t\frac{\partial p^{n+1}}{\partial x_i} - \frac{1}{\rho}(1-\alpha)\Delta t\frac{\partial p^n}{\partial x_i}, \tag{3}$$

where $H\left(u_i^n, u_i^{n+1}\right)$ includes convection, the viscous and the source terms, and $\alpha = 0.5$ (Crank–Nicolson). Equation (3) is solved, which gives u_i^{n+1}, which does not satisfy continuity. An intermediate velocity field is computed by subtracting the implicit part of the pressure gradient, i.e.,

$$u_i^* = u_i^{n+1} + \frac{1}{\rho}\alpha\Delta t\frac{\partial p^{n+1}}{\partial x_i}. \tag{4}$$

Taking the divergence of Eq. (4), requiring that continuity (for the face velocities that are obtained by linear interpolation) should be satisfied on level $n+1$, i.e., $\partial u_{i,f}^{n+1}/\partial x_i = 0$, we obtain

$$\frac{\partial^2 p^{n+1}}{\partial x_i \partial x_i} = \frac{\rho}{\Delta t\alpha}\frac{\partial u_{i,f}^*}{\partial x_i}. \tag{5}$$

The numerical procedure at each time step can be summarized as follows:[31]

1. Solve the discretized filtered Navier–Stokes equation for u, v, and w.
2. Create an intermediate velocity field u_i^* from Eq. (4).
3. The Poisson equation [Eq. (5)] is solved with an efficient multigrid method.[32]
4. Compute the face velocities (which satisfy continuity) from the pressure and the intermediate velocity as

$$u_{i,f}^{n+1} = u_{i,f}^* - \frac{1}{\rho}\alpha\Delta t\left(\frac{\partial p^{n+1}}{\partial x_i}\right)_f. \tag{6}$$

5. Steps 1–4 is performed until convergence (normally two or three iterations) is reached. The convergence for the velocities is 10^{-7} and 10^{-5} for pressure. The residuals are computed using the $L1$ norm, and they are scaled with the integrated streamwise volume flux (continuity equation) and momentum flux (momentum equations).
6. Next time step.

Note that although no explicit dissipation is introduced to prevent odd–even decoupling, an implicit dissipation is present. The intermediate velocity field is computed at the *cell centers* [see Eq. (4)] subtracting a pressure gradient. When, after having solved the pressure Poisson equation, the face velocity field is computed, the pressure gradient at the *faces* [see Eq. (6)] is added. This is very similar to the Rhie–Chow dissipation.[33]

B. Body force generated by single DBD actuator

The Shyy model is considered to simulate the effect of a DBD actuator. The Shyy model creates an electric field vector, $\mathbf{E}$, generated by a DBD plasma actuator, which is given as

$$E(y,z) = E_0 - \frac{E_0 - E_b}{b}z - \frac{E_0 - E_b}{b\tan(\theta)}y. \tag{7}$$

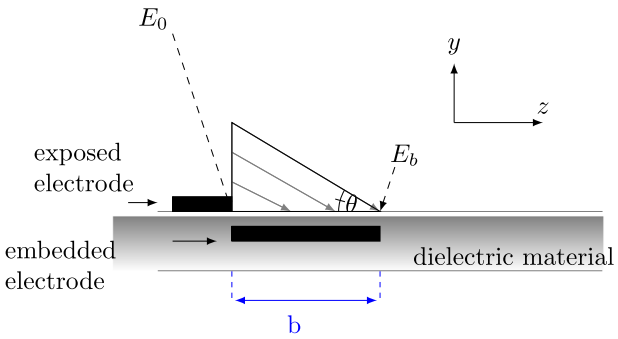

FIG. 1. Shyy model illustration. Electric field strength, $E(y, z)$.

Equation (7) is divided into wall-normal and spanwise components, multiplied by a dimensional term Dc^* that defines the strength of the electrical force,

$$F_z(y,z) = Dc^* E(y,z)\cos\theta, \tag{8}$$

$$F_y(y,z) = Dc^* E(y,z)\sin\theta. \tag{9}$$

$Dc^* = q_0^* E_0^*$, where q_0^* is the maximum electron charge density (C/m^3) and E_0^* is the maximum electric field strength (N/m^3). E_0 is the non-dimensional maximum electric field strength, which is defined by $E_0 = E_0^*/E_{ref}$, where $E_{ref} = E_0^*$.[34] Thus, $E_0 = 1.0$, which decays along the embedded electrode that ceases on the other edge and takes its breakdown strength, E_b (see Fig. 1). In this study, E_b is set to 0.1. The parameter b is the length of the plasma area, and the height of the plasma area is thus set to $b\tan(\theta)$ (see Fig. 1).

C. Validation of the body force

The numerical model is compared with the experimental data in a stagnant flow with a single DBD actuator. Experimental and numerical results were obtained with a single DBD actuator. Experimental study is performed by Benard *et al.*[8] for an applied voltage of 12 kV and an AC frequency of 1000 Hz.

A two-dimensional study in a channel is performed (see Fig. 2). Equations (8) and (9) are applied as a body force in two-dimensions

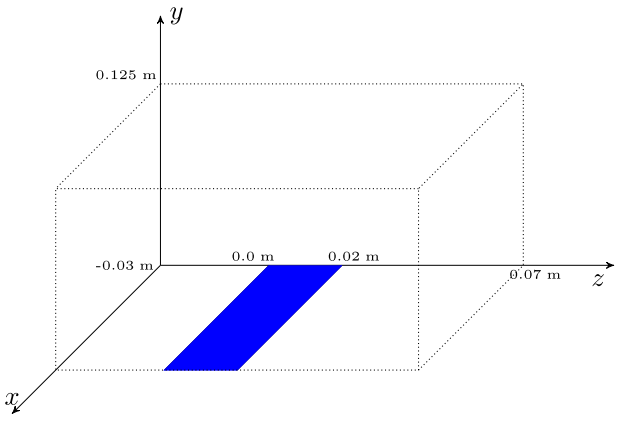

FIG. 2. The location of the embedded electrode for the numerical study.

(y and z), and the simulation is carried out in time until steady state is reached. Slip boundary conditions are applied at the top boundary ($y = 0.125$ m) and at $z = 0$ m and $z = 0.07$ m. No-slip boundary conditions are applied at $y = 0$. The viscosity $\nu = 1.81 \times 10^{-5}$ m^2/s and density $\rho = 1.25$ kg/m^3 are taken for ionized air. We have applied very low θ, approximately zero. Then, F_y in Eq. (9) is much smaller (~10 times smaller) than F_z in Eq. (8). In our previous studies, for the low θ, we did not observe any difference between the results obtained, respectively, by applying Eq. (8) together with Eq. (9) and by applying Eq. (8) alone. In this study, we have thus applied only the plasma-aligned (spanwise for DNS in Chapter III) component of the force. In this case, θ is absent in Eq. (10) (see p. 13). This is similar to the model by Greenblatt *et al.*,[35] where they applied a mean body force that acts only in the plasma-aligned direction. The domain size is 125×100 mm^2 (see Fig. 2) with grid sizes 98×298 ($y \times z$) for the wall-normal and plasma-aligned directions, respectively. The minimum and maximum grid sizes are $\Delta y_{min} = 0.000\,25$ m and $\Delta y_{max} = 0.0025$ m with a stretching of $\Delta y_i/\Delta y_{i-1} = 1.035$ in the wall-normal direction. In the spanwise direction, uniform cells are used with $\Delta z = 0.000\,33$ m. The oscillating force is applied in the plasma region (0.0 m $< z < 0.02$ m, 0.0 m $< y < 0.0028$ m). The length of the plasma is $b = 20$ mm, and the location of the plasma is illustrated in blue in Fig. 2. The plasma region is covered by 30×6 cells ($z \times y$) in the plasma-aligned and wall-normal directions, respectively.

The thickness of the exposed electrode is set to be ideally zero. The predicted velocities of the ionized air flow exhibit very similar behavior as compared to the experimental data (see Fig. 3, where the left-hand side figures illustrate the experimental data[8] and the right-hand side figures for the numerical study). The plasma actuators create a negative wall-normal velocity upstream and a positive wall-normal velocity downstream of the embedded electrode [Figs. 3(a) and 3(b)]. The negative area entrains the flow toward the wall, as shown in Fig. 3(a), and the positive area creates a wall jet toward downstream with a velocity parallel to the actuator, as disclosed in [Fig. 3(b)]. Large vorticity is created in the shear layer above the embedded electrode [Fig. 3(c)]. In the experimental study, the maximum of the plasma-aligned velocity is 1.8 m/s, and the wall-normal velocity is about half of that, 0.9 m/s. In the numerical study, the maximum of the plasma-aligned velocity is 1.6 m/s, and the wall-normal velocity is about 0.6 m/s. The vorticity magnitude is 1400 1/s for the experimental case, while 3000 1/s for the numerical study. The color scale in Fig. 3 is based on the maximum and minimum levels of the numerical result. It should be noted that the experimental data are used here to demonstrate the proof of the suggested numerical modeling. In the numerical study, we obtain matching velocity patterns compared to the experiments. This suggests that the numerical model presented is relevant to the modeling of the ionized air flow generated by the DBD plasma actuator.

D. Multiple plasma actuators for DNS

1. Force created by sinusoidal applied plasma

In DNS, a spanwise oscillating body force is created by multiple plasma actuators, which are aligned in the spanwise direction (Fig. 4). Only a spanwise oscillating component of the body force, F_z^+,

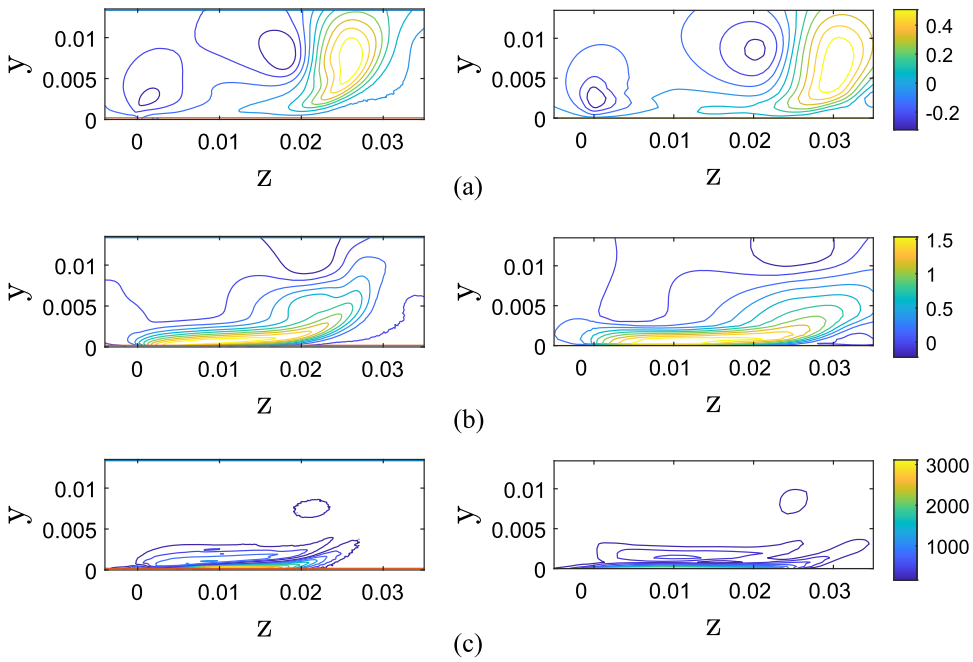

FIG. 3. (a) Wall-normal velocity, *v*, (b) plasma-aligned velocity, *w*, and (c) vorticity for the experimental study[8] in the left-hand side and numerical study in right-hand side.

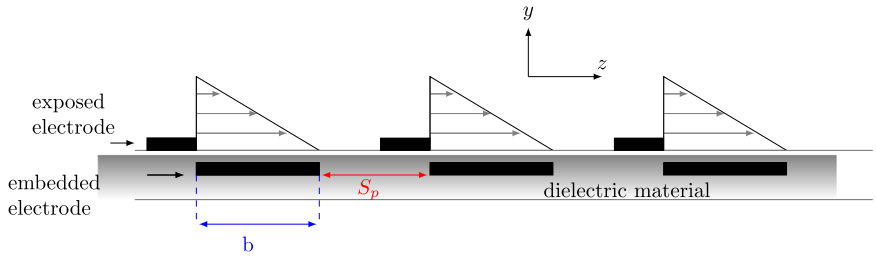

FIG. 4. Electric field, *E*(*y*, *z*), illustration for the multiple actuator case.

is applied ($F_y^+ = 0$). Equation (8) is modified by applying a sinusoidal variation in the spanwise direction (Fig. 5),

$$F_z^+(y,z) = Dc\, E(y,z)\ \sin(2\pi x^+/\lambda_x^+). \tag{10}$$

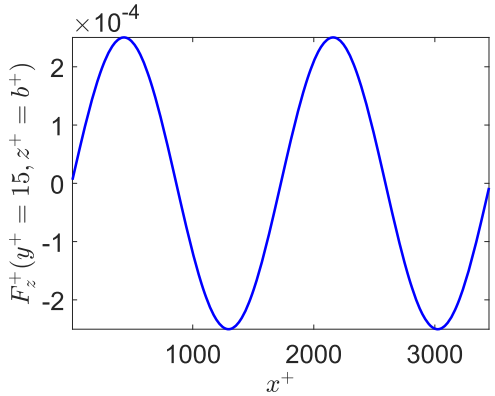

FIG. 5. Force along the streamwise direction is a sinusoidal directed to the spanwise direction. $Re_\tau = 550$.

$Dc = \frac{q_0^* E_0^* \delta}{\rho u_\tau^2}$ represents the ratio of the electrical force to the inertial force, where δ, ρ, and u_τ, are half the channel height, fluid density, and the friction velocity, respectively. The length of the plasma area, *b*, is 13 cells, which corresponds to $b^+ = \frac{bu_\tau}{\nu} = 28.3$ for $Re_\tau = 180$ and $b^+ = 87.3$ for $Re_\tau = 550$, which defines the maximum width of the plasma in the spanwise direction (see Fig. 1). The extent of the plasma area in the wall-normal direction is $0 < y^+ < 8$, which corresponds to 7 and 4 cells for $Re_\tau = 180$ and $Re_\tau = 550$, respectively. Three different numerical test cases are studied. The force created by the numerical set up mimics the experimental study by Benard *et al.*[30] A continuous force in the spanwise direction is used in the first case [see Figs. 6(a) and 6(b)]. In the second test case, a discrete force is created by applying a spanwise spacing, S_p, of one plasma length, b^+, in between the array of embedded electrodes, namely, $S_p = b^+$ [see Figs. 6(c) and 6(d)]. $Dc = 120.0$ is used for the continuous case, and $Dc = 60.0$ is used for the discrete case. For the discrete design of the actuators, we have observed drag increase for higher Dc values. For $Re_\tau = 180$, for the continuous case, keeping all the other parameters same, a lower drag reduction is observed for the lower *Dc* (a drag reduction of 2.8%, 7%, and 8.8% for $Dc = 50$, 60, and 90, respectively), and we also observed a slightly lower drag reduction

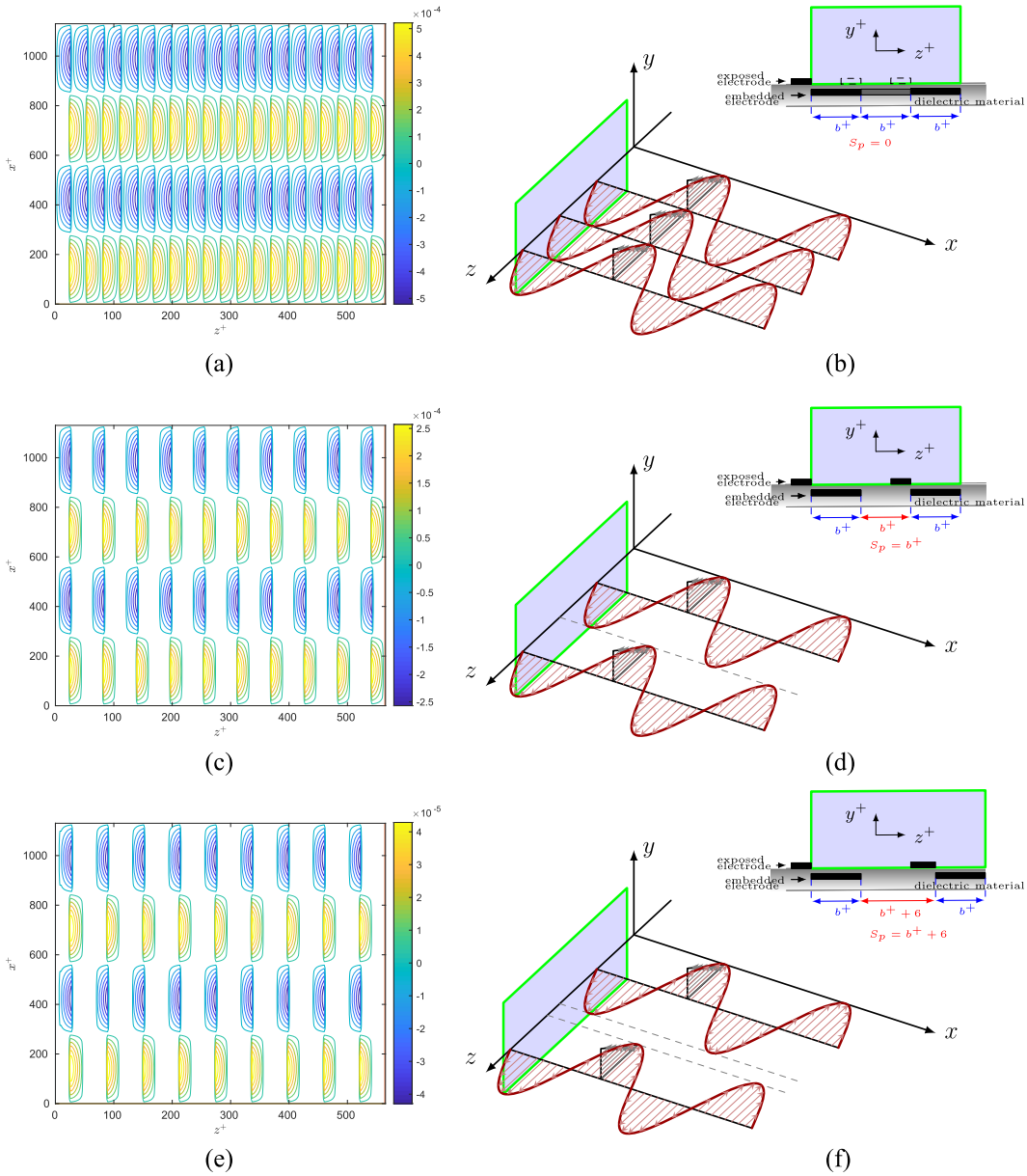

FIG. 6. Spatially oscillating plasma force, F_z^+, implemented in DNS studies. (a) Contours of F_z^+, continuous case. (b) Three-dimensional view of F_z^+, continuous case. (c) Contours of F_z^+, discrete plasma areas without space between them. (d) Three-dimensional view of F_z^+, discrete plasma areas without space between them. (e) Contours of F_z^+, discrete plasma areas with a spanwise spacing of $z^+ = b^+ + 6$. (f) Three-dimensional view of F_z^+, discrete plasma areas with a spanwise spacing of $z^+ = b^+ + 6$.

for $Dc = 150$. The drag reduction is calculated from the wall shear stress, τ_w, of force and no-force cases,

$$Dr = \frac{\tau_{w_0} - \tau_{w_f}}{\tau_{w_0}} \times 100,$$

where τ_{w_0} and τ_{w_f} are the wall shear stresses on the lower wall for no-force and force cases, respectively. The force oscillates spatially in the streamwise direction, and the values range between $\pm 3 \times 10^{-4}$ and $\pm 5.5 \times 10^{-5}$ for the continuous and the discrete cases, respectively. 19 and 10 actuators are used in the spanwise direction for the continuous and the discrete force cases, respectively. For the third case, there is a spanwise spacing of $z^+ = b^+ + 6$ between the array of embedded electrodes in Figs. 6(e) and 6(f), using nine actuators; all the other parameters are kept the same as for the discrete force case in Figs. 6(c) and 6(d). The streamwise wavelength of the force for all three test cases is $\lambda_x^+ = 180\pi$. For $Re_\tau = 550$, we applied the

same parameters as the continuous case with $Re_\tau = 180$ [see Figs. 6(a) and 6(b)].

2. DNS settings

In DNS of fully developed turbulent channel flows, a constant volumetric driving force is used in the streamwise momentum equation by which the frictional Reynolds number, $Re_\tau = 180$, is prescribed (based on the driving pressure gradient and channel half width). Periodic boundary conditions are used in the streamwise and spanwise directions, while the usual no-slip boundary conditions are enforced at the walls. The domain size is $2\pi\delta \times 2\delta \times \pi\delta$ with grid sizes $98 \times 98 \times 258$, in the streamwise, wall-normal, and spanwise directions, respectively. The grid resolution is $\Delta x^+ \approx 11$, $\Delta z^+ \approx 2.2$. A stretching of 1.035 is used in the wall-normal direction. The validity of the method for the higher Reynolds number is investigated at a frictional Reynolds number of $Re_\tau = 550$ with a domain size of $2\pi\delta \times 2\delta \times \pi\delta$ and a grid size of $258 \times 98 \times 258$ in the streamwise, wall-normal, and spanwise directions, respectively. The grid resolution is $\Delta x^+ \approx 13$, $\Delta z^+ \approx 6$. A stretching of 1.035 is used in the wall-normal direction. Unless otherwise stated, the results are presented below for $Re_\tau = 180$.

The nondimensional time step was kept smaller than $\Delta t^+ = \Delta t u_\tau^2/\nu = 0.6$. The variables u, v, and w, represent the streamwise, wall-normal, and spanwise velocities, respectively. Before applying any control, all simulations are allowed to reach a fully developed turbulent flow state. Plasma-generated force is applied to the lower wall only. The results are, unless otherwise stated, averaged in time and in all homogeneous directions (i.e., x and z); the average is denoted by an overbar $(\bar{\cdot})$.

III. RESULTS AND DISCUSSION

Figures 7(a)–7(d) show the Reynolds shear stresses for the force cases at $Re_\tau = 180$, and $Re_\tau = 550$, respectively, which are compared with the no-force case. A drag reduction of 13% and 4% is observed in Figs. 7(a) and 7(b), respectively. Figure 7(c) shows the Reynolds shear stress for the case with the discrete plasma area with a spanwise spacing of $z^+ = b^+ + 6$, in which we did not observe any drag reduction. For the continuous case at $Re_\tau = 550$, a drag reduction of 11% is obtained; the Reynolds shear stress is given in Fig. 7(d).

Drag histories show a clear skin friction reduction for the force applied lower wall (given in blue), compared to the upper wall for the continuous force cases at $Re_\tau = 180$ and $Re_\tau = 550$ shown in Figs. 8(a) and 8(b), respectively. In the following analysis, unless otherwise stated, the results are given for the continuous force case at $Re_\tau = 180$.

Figure 9(a) presents the mean velocity for the force and the no-force cases, compared with the DNS data.[36] In Fig. 9(a), for the applied-force case, the viscous sublayer region intercepts with the log-law layer at a higher y^+ level, the higher shift of the intercept

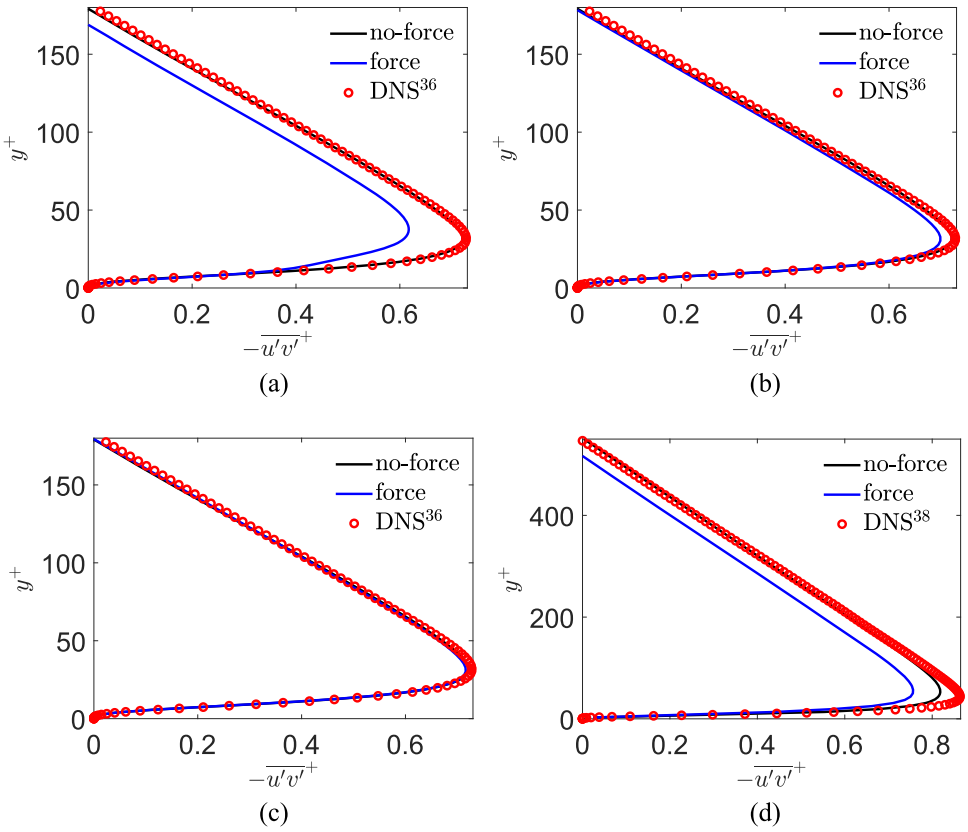

FIG. 7. Reynolds shear stresses. (a) Continuous force case, $Re_\tau = 180$. (b) Discrete plasma areas without space between them, $Re_\tau = 180$. (c) Discrete plasma areas with a spanwise spacing of $z^+ = b^+ + 6$, $Re_\tau = 180$. (d) Continuous force case, $Re_\tau = 550$.

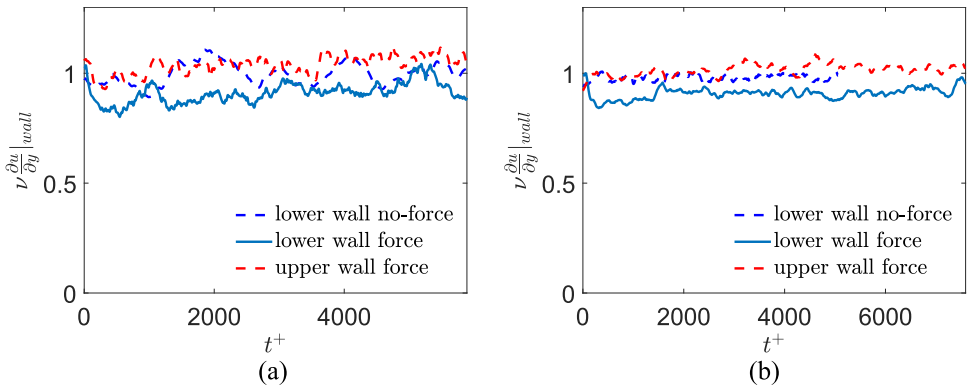

FIG. 8. Drag histories in time: (a) Re_τ = 180 and (b) Re_τ = 550.

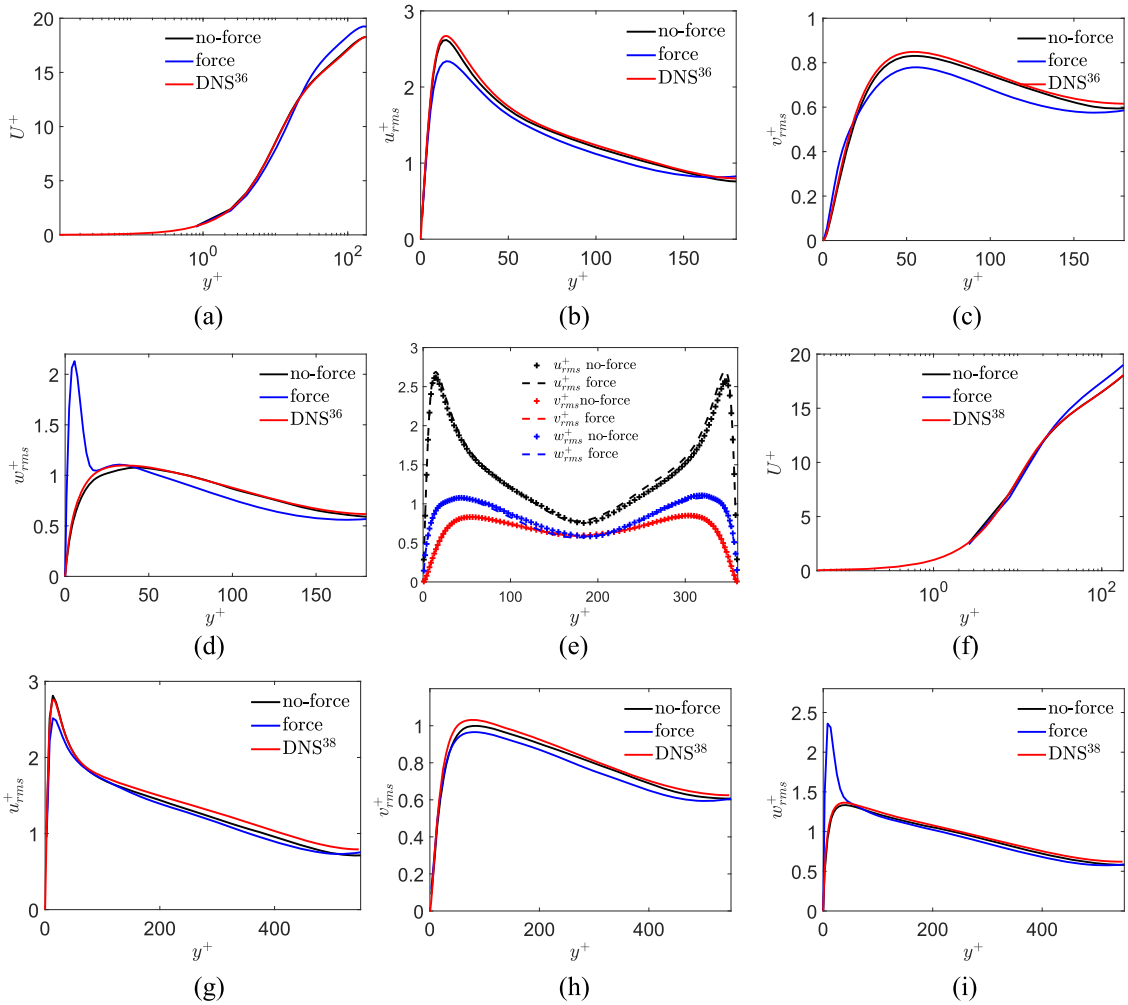

FIG. 9. Mean and fluctuation velocities. (a) Mean velocity, Re_τ = 180. (b) Streamwise velocity rms, u^+_{rms}, Re_τ = 180. (c) Wall-normal velocity rms, v^+_{rms}, Re_τ = 180. (d) Spanwise velocity rms, w^+_{rms}, Re_τ = 180. (e) Velocity rms for the discrete plasma areas with a spanwise spacing of $z^+ = b^+ + 6$, Re_τ = 180. (f) Mean velocity, Re_τ = 550. (g) Streamwise velocity rms, u^+_{rms}, Re_τ = 550. (h) Wall-normal velocity rms, v^+_{rms}, Re_τ = 550. (i) Spanwise velocity rms, w^+_{rms}, Re_τ = 550.

point is the result of the increase in the viscous sublayer thickness.[37] Slightly lower streamwise velocity fluctuations, u_{rms}, and wall-normal velocity fluctuations, v_{rms}, are observed for the applied-force case compared to the no-force case [Figs. 9(b) and 9(c)]. The plasma force creates an additional momentum in the vicinity of the wall in both the wall-normal and spanwise directions. The created momentum is higher in the spanwise direction compared to the wall-normal since a high speed near-wall jet is created in the spanwise direction [Figs. 9(c) and 9(d)]. For the applied-force case, the spanwise velocity fluctuations, w_{rms}, are higher at the vicinity of the wall, up to a level of $y^+ \approx 15$ [see Fig. 9(d)]. Figure 9(e) presents a comparison of the velocity fluctuations for the case with discrete actuators by a spanwise spacing of $z^+ = b^+ + 6$ and the no-force. Similar to shear stresses, Fig. 7(c), the velocity rms values for the spanwise spacing case follow the no-force case. The mean velocity profile exhibits a shift to a higher wall-normal location, similar as for $Re_\tau = 180$, which is shown in Fig. 9(f), compared with the DNS data.[38] For $Re_\tau = 550$, we obtain similar rms velocity profiles as $Re_\tau = 180$ [Figs. 9(g)–9(i)].

An estimation on the change in the vortex structures can be made by comparing the streamwise vorticity fluctuations for the applied-force and no-force cases. It has been shown that the spanwise oscillating Lorentz force modifies the mean vortex structure to an elliptic and much smaller shape.[2] A closer distance between the rms of the streamwise vorticity fluctuations' minima and maxima locations is observed, which indicates that the mean vortex structure is shrinking to a smaller form for the applied-force case [see Figs. 10(a) and 10(b)]. The two terms of the streamwise vorticity, $\partial w'/\partial y$ and $\partial v'/\partial z$, are given in Fig. 10(c), which shows that the term $\partial w'/\partial y$ is responsible for the rise of the streamwise vorticity fluctuations, which also determine the maxima and minima locations. The forcing gives rise to an increase in $\partial w'/\partial y$, which explains why $\omega'_{x_{rms}}$ is larger close to the wall in the applied-force case compared to the no-force case. A similar change in the streamwise vorticity is observed for $Re_\tau = 550$ [Fig. 10(d)] as for $Re_\tau = 180$. We did not observe any modification on the streamwise rms vorticity and its components for the case discrete plasma areas with a spanwise spacing of $z^+ = b^+ + 6$ [see Fig. 10(e)].

The "streak cycle" that represents the regeneration cycle of low-speed streaks and streamwise vortices is investigated by Hamilton *et al.*[39] and Jiménez and Pinelli.[14] In their study, they showed that the cycle is governed by the streak instability, which generates tilted streamwise vortices. In turn, the streamwise vortices assemble low-speed fluid and generate low velocity streaks. These streaks undergo wavy motions and lead to streak instability.

Two-point correlations are very effective for understanding the structure of the flow. In Figs. 11 and 12, we depict two-point correlations for the streamwise and spanwise velocities for the lower and upper wall. Since the force is applied only in the lower half of the channel, the two-point correlations in the upper half are very similar for the applied-force and the no-force cases [Figs. 11(b), 11(d), 12(b), and 12(d)]. Streamwise velocity two-point correlation, $R_{uu}(\hat{z})$, which carries information on the mean spacing between the streaks, is investigated to identify the effect by the spanwise oscillated plasma

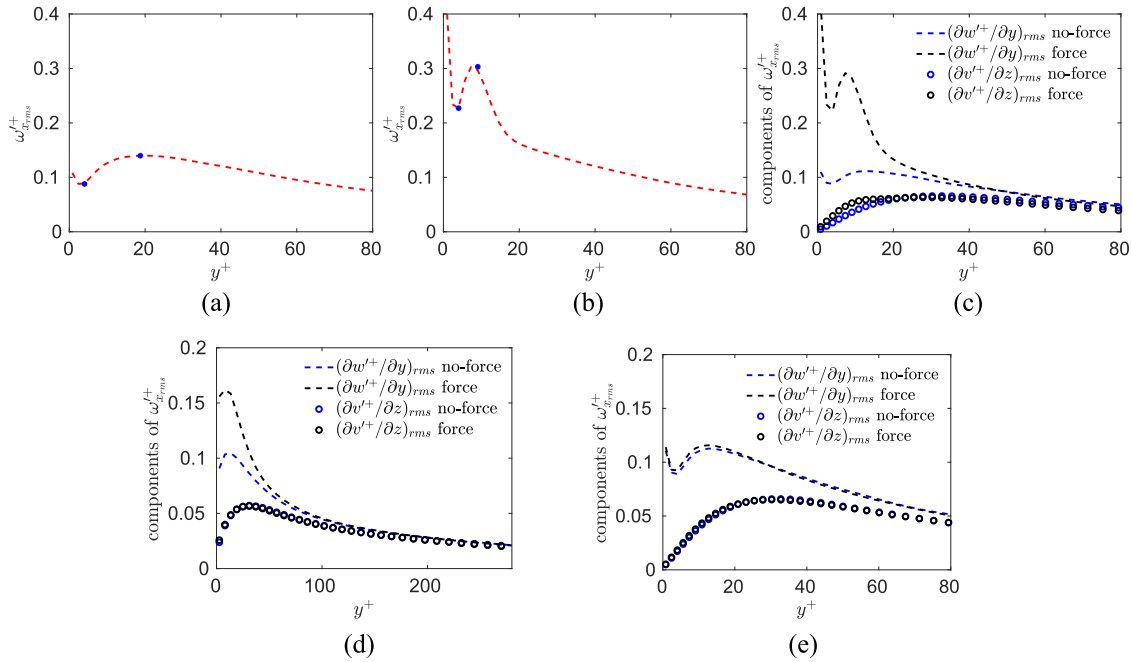

FIG. 10. Streamwise vorticity fluctuations. (a) Streamwise vorticity fluctuations, $\omega'^+_{x_{rms}}$, no-force case, $Re_\tau = 180$. (b) Streamwise vorticity fluctuations, $\omega'^+_{x_{rms}}$, force case, $Re_\tau = 180$. (c) The two terms of $\omega'^+_{x_{rms}}$. $Re_\tau = 180$. (d) The two terms of $\omega'^+_{x_{rms}}$. $Re_\tau = 550$. (e) The two terms of $\omega'^+_{x_{rms}}$ for the discrete plasma areas with a spanwise spacing of $z^+ = b^+ + 6$. $Re_\tau = 180$.

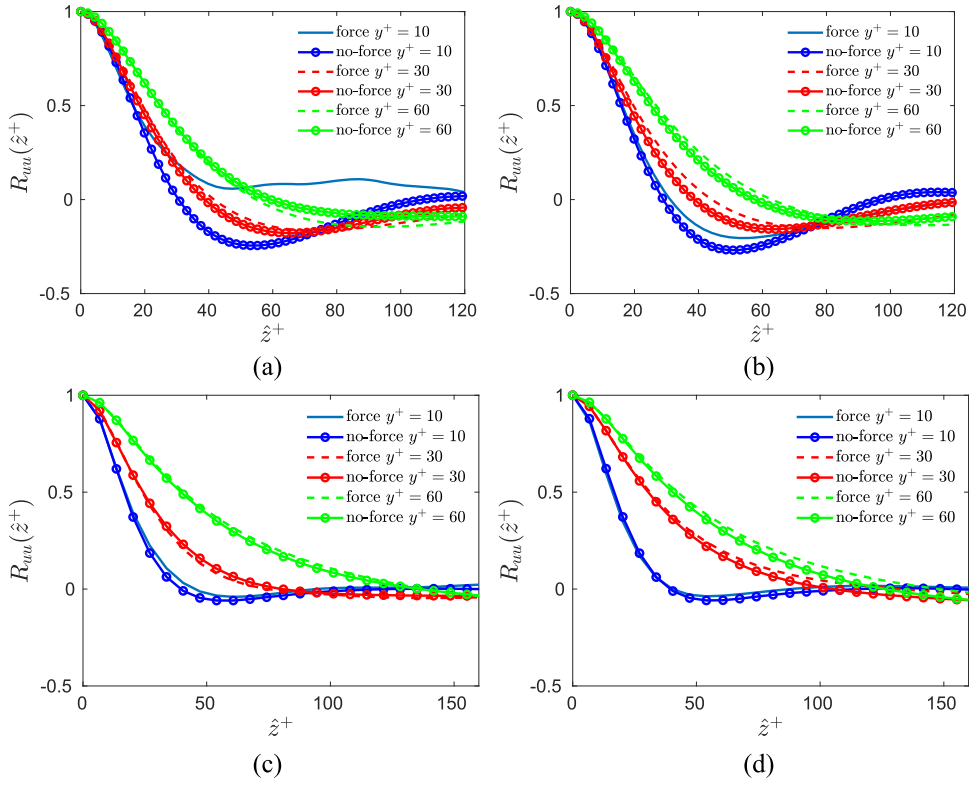

FIG. 11. Streamwise two-point velocity correlation. (a) Lower wall. Re_τ = 180. (b) Upper wall. Re_τ = 180. (c) Lower wall. Re_τ = 550. (d) Upper wall. Re_τ = 550.

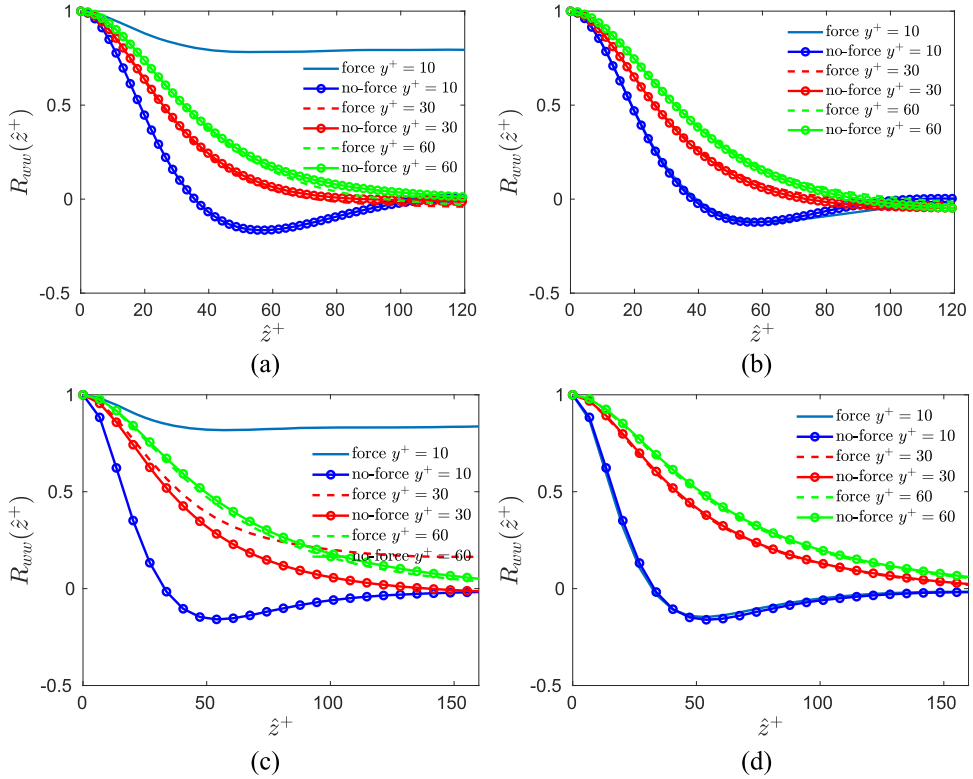

FIG. 12. Spanwise two-point velocity correlation. (a) Lower wall. Re_τ = 180. (b) Upper wall. Re_τ = 180. (c) Lower wall. Re_τ = 550. (d) Upper wall. Re_τ = 550.

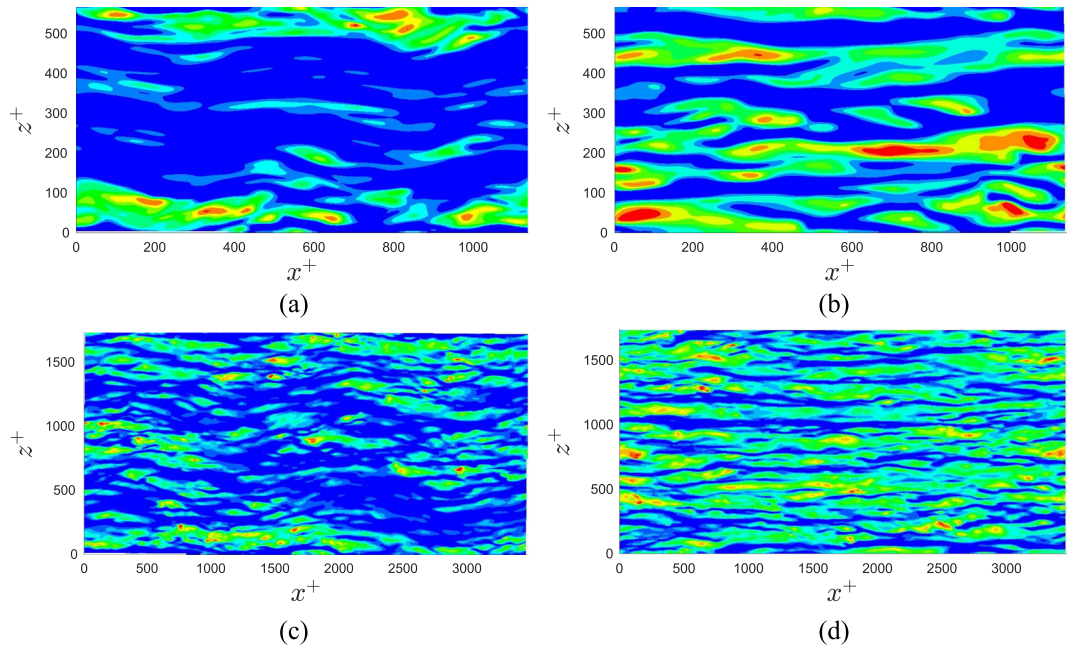

FIG. 13. Streamwise velocity (u) contours near the lower wall for force applied and no-force cases at $y^+ = 10$. Blue color indicates low-speed streaks, and yellow-red for high-speed streaks. Contour levels are 7–14 for $Re_\tau = 180$ and 6–16 for $Re_\tau = 550$. (a) Lower wall (force applied). $Re_\tau = 180$. (b) Lower wall (no-force). $Re_\tau = 180$. (c) Lower wall (force applied). $Re_\tau = 550$. (d) Lower wall (no-force). $Re_\tau = 550$.

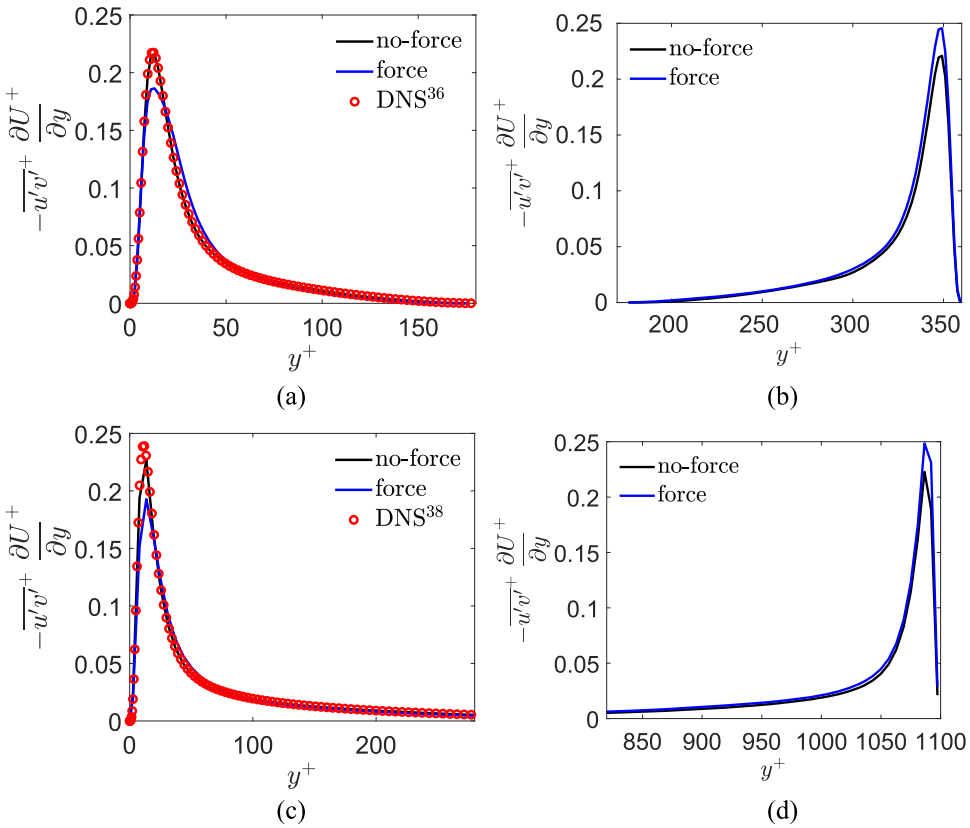

FIG. 14. Turbulence production. (a) Lower wall. $Re_\tau = 180$. (b) Upper wall. $Re_\tau = 180$. (c) Lower wall. $Re_\tau = 550$. (d) Upper wall. $Re_\tau = 550$.

force on the streaky structures. The location of the negative minimum of $R_{uu}(\hat{z})$ provides an estimate of the mean separation between the high and the low speed fluid; the mean spacing between the streaks of high and low speed fluids is roughly twice of that separation.[40] In Fig. 11(a), the streamwise velocity two-point correlations, $R_{uu}(\hat{z})$, are shown near the lower wall for $Re_\tau = 180$. While the minimum value for the no-force correlation is observed approximately at $z^+ = 54$ for $y^+ = 10$, the applied-force case does not exhibit any minimum for $y^+ = 10$, which indicates the absence of streaky structures[37] or more stable or weak streaky structures near the wall compared to the no-force case.[14] The absence of a minimum may also indicate an enlargement of the streaks in the spanwise direction.[37,41] However, for $Re_\tau = 550$, streamwise velocity two-point correlations, $R_{uu}(\hat{z})$, do not show a strong change in streaky structures but a faint difference at $y^+ = 10$ compared to the no-force case [Fig. 11(c)]. The discussion below gives further insight into the modification of the turbulent structures near the wall.

The presence of a minimum in the spanwise velocity two-point correlation profiles, $R_{ww}(\hat{z})$, was originally believed to be related to the separation of two streamwise vortices.[41] Later on, the cause of this minimum in $R_{ww}(\hat{z})$ was found to be impingement or splattings of high-speed fluid at the wall.[16,40] In Figs. 12(a) and 12(c), the spanwise velocity two-point correlations, $R_{ww}(\hat{z})$, are shown near the lower wall for $Re_\tau = 180$ and $Re_\tau = 550$, respectively. It is observed that for neither Reynolds numbers is there any minimum for $R_{ww}(\hat{z})$ at $y^+ = 10$, which indicates a reduction at splattings at the wall [Figs. 12(a) and 12(c)].

$R_{ww}(\hat{z})$ profiles show a modification at $y^+ = 30$ for $Re_\tau = 550$ for the force case compared to the no-force case, while it follows the no-force case for $Re_\tau = 180$. It has been shown in Fig. 9(d) that the spanwise velocity fluctuations, w_{rms}, are affected in the vicinity of the wall up to a level of $y^+ \approx 15$ for $Re_\tau = 180$, while it is affected up to a level of $y^+ \approx 50$ for $Re_\tau = 550$. This is also in agreement with the streamwise vorticity fluctuations given in Figs. 10(c) and 10(d) for the $Re_\tau = 180$ and $Re_\tau = 550$ cases, respectively.

Figure 13 presents the streamwise velocity, u, contours at $y^+ = 10$ over the lower wall for the no-force and force cases. The force effect is clearly visible at the lower wall for $Re_\tau = 180$ [Fig. 13(a)], where high speed streaks have disappeared in the mid area of the channel in the spanwise direction, as compared to the no-force case [Fig. 13(b)]. The same effect is observed at the lower wall for $Re_\tau = 550$ [Fig. 13(c)] compared to the no-force case [Fig. 13(d)].

Finally, we present the turbulence productions in Fig. 14. A reduction is observed near the lower wall, and an enhancement is observed near the upper wall in the applied-force case compared to the no-force case, as shown in Figs. 14(a) and 14(b) and Figs. 14(c) and 14(d) for $Re_\tau = 180$ and $Re_\tau = 550$, respectively.

IV. CONCLUSIONS

In this study, the effect of a spanwise oscillated body force is explored and demonstrated, being a very effective approach to manipulate turbulent boundary layers and to achieve drag reduction. The body force is created by a series of spanwise aligned plasma areas that mimics DBD plasma actuators.

A single plasma actuator is studied first, in a stagnant flow, and the created velocities and vorticities are compared with the experimental results in the literature. Good agreement is obtained. Then a DNS study of fully developed turbulent channel flow was carried out by introducing a spanwise oscillating plasma force near the lower wall. The plasma force is created by spanwise aligned plasma areas. Three different cases have been studied at a frictional Reynolds number of $Re_\tau = 180$, namely, a continuous force, a force created by discrete plasma areas with a spanwise spacing of b, and a force created by discrete plasma areas with a spanwise spacing of $z^+ = b^+ + 6$ (see Fig. 6). We have achieved a drag reduction of 13%, 4%, and 0%, respectively. We have also applied the continuous case to a higher Reynolds number, $Re_\tau = 550$, and 11% of drag reduction is attained.

We found that in the applied-force case, the streamwise velocity two-point correlation, $R_{uu}(z)$, profile does not exhibit any minima at $y^+ = 10$ for the case at $Re_\tau = 180$ [Fig. 11(a)]. Moreover, the spanwise two-point velocity correlation, $R_{ww}(z)$, not exhibit any minima for either $Re_\tau = 180$ or $Re_\tau = 550$, which indicates an absence of the streak formations in the vicinity of the wall [Figs. 12(a) and 12(c)]. This observation is supported by contours of the streamwise velocity, u, at $y^+ = 10$ for the lower and upper walls, which clearly shows the absence of the high-speed streak formations at the lower wall (see Fig. 13).

Finally, we analyzed the turbulence production. We observed a lower turbulence production near the lower wall in the applied-force case compared with the no-force case, while the situation is reversed near the upper wall for both the low and high Reynolds numbers (see Fig. 14).

Overall, we believe that the analysis has highlighted some important aspects for the future of drag reduction studies. It shows that the DBD-generated spanwise forcing is able to achieve effective drag reduction by manipulating near-wall turbulent structures in the boundary layer. The use of DBD plasma actuators for their light structures is of great interest in flow control for engineering applications.

ACKNOWLEDGMENTS

This work was supported partially by the European Commission through the Research and Innovation action DRAGY (Grant Agreement No. 690623) and Chalmers University, Energy Area of Advance.

DATA AVAILABILITY

The data that support the findings of this study are available from the corresponding author upon reasonable request.

REFERENCES

[1] L. Zhang, X. Shan, and T. Xie, "Active control for wall drag reduction: Methods, mechanisms and performance," IEEE Access **8**, 7039–7057 (2020).
[2] A. Altıntaş and L. Davidson, "Direct numerical simulation analysis of spanwise oscillating Lorentz force in turbulent channel flow at low Reynolds number," Acta Mech. **228**, 1269–1286 (2017).

[3]W. Jung, N. Mangiavacchi, and R. Akhavan, "Suppression of turbulence in wall-bounded flows by high-frequency spanwise oscillations," Phys. Fluids A **4**, 1605–1607 (1992).
[4]P. Xu and K. S. Choi, "Boundary layer control for drag reduction by Lorentz forcing," in *IUTAM Symposium on Flow Control and MEMS*, edited by J. F. Morrison, D. M. Birch, and P. Lavoie (Springer, 2008), pp. 259–265.
[5]H. R. Velkoff and J. Ketcham, "Effect of an electrostatic field on boundary-layer transition," AIAA J. **6**, 1381–1383 (1968).
[6]J. Roth, D. Sherman, and S. Wilkinson, "Boundary layer flow control with a one atmosphere uniform glow discharge surface plasma," in *36th AIAA Aerospace Sciences Meeting and Exhibit* (AIAA, 1998), p. 328.
[7]N. Qin, J. Periaux, and G. Bugeda, *Advances in Effective Flow Separation Control for Aircraft Drag Reduction: Modeling, Simulations and Experimentations* (Springer Nature, 2019), Vol. 52.
[8]N. Benard, M. Caron, and E. Moreau, "Evaluation of the time-resolved EHD force produced by a plasma actuator by particle image velocimetry: A parametric study," J. Phys.: Conf. Ser. **646**, 012055 (2015).
[9]W. Shyy, B. Jayaraman, and A. Andersson, "Modeling of glow discharge-induced fluid dynamics," J. Appl. Phys. **92**, 6434–6443 (2002).
[10]T. Jukes, K.-S. Choi, G. Johnson, and S. Scott, "Turbulent drag reduction by surface plasma through spanwise flow oscillation," in *3rd AIAA Flow Control Conference* (AIAA, 2006), p. 3693.
[11]T. N. Jukes, "Turbulent drag reduction using surface plasma," Ph.D. thesis, University of Nottingham, 2007.
[12]O. Mahfoze and S. Laizet, "Skin-friction drag reduction in a channel flow with streamwise-aligned plasma actuators," Int. J. Heat Fluid Flow **66**, 83–94 (2017).
[13]T. W. Berger, J. Kim, and C. Lee, "Turbulent boundary layer control utilizing the Lorentz force," Phys. Fluids **12**, 631–649 (2000).
[14]J. Jiménez and A. Pinelli, "The autonomous cycle of near-wall turbulence," J. Fluid Mech. **389**, 335–359 (1999).
[15]J. Kim, "Physics and control of wall turbulence for drag reduction," Philos. Trans. R. Soc., A **369**, 1396–1411 (2011).
[16]J. Kim, "Study of turbulence structure through numerical simulations: The perspective of drag reduction," AGARD Report No. R-786, AGARD FDP/VKI Special Course on "Skin Friction Drag Reduction," 2–6 March 1992, VKI, Brussels, 1992.
[17]S. K. Robinson, "Coherent motions in the turbulent boundary layer," Annu. Rev. Fluid Mech. **23**, 601–639 (1991).
[18]L. Agostini, E. Touber, and M. A. Leschziner, "Spanwise oscillatory wall motion in channel flow: Drag-reduction mechanisms inferred from DNS-predicted phase-wise property variations at $Re_\tau = 1000$," J. Fluid Mech. **743**, 606–635 (2014).
[19]M. Abbassi, W. Baars, N. Hutchins, and I. Marusic, "Skin-friction drag reduction in a high-Reynolds-number turbulent boundary layer via real-time control of large-scale structures," Int. J. Heat Fluid Flow **67**, 30–41 (2017).
[20]J. Jiménez, "The largest scales of turbulent wall flows," in *CTR Annual Research Briefs* (Stanford University, 1998), Vol. 137, p. 54.
[21]R. J. Adrian, C. D. Meinhart, and C. D. Tomkins, "Vortex organization in the outer region of the turbulent boundary layer," J. Fluid Mech. **422**, 1–54 (2000).
[22]J. Jiménez, J. C. Del Álamo, and O. Flores, "The large-scale dynamics of near-wall turbulence," J. Fluid Mech. **505**, 179–199 (2004).
[23]N. Hutchins and I. Marusic, "Evidence of very long meandering features in the logarithmic region of turbulent boundary layers," J. Fluid Mech. **579**, 1–28 (2007).
[24]R. Mathis, N. Hutchins, and I. Marusic, "Large-scale amplitude modulation of the small-scale structures in turbulent boundary layers," J. Fluid Mech. **628**, 311–337 (2009).
[25]P. Schlatter and R. Örlü, "Quantifying the interaction between large and small scales in wall-bounded turbulent flows: A note of caution," Phys. Fluids **22**, 051704 (2010).
[26]R. Mathis, I. Marusic, N. Hutchins, and K. Sreenivasan, "The relationship between the velocity skewness and the amplitude modulation of the small scale by the large scale in turbulent boundary layers," Phys. Fluids **23**, 121702 (2011).
[27]B. Ganapathisubramani, N. Hutchins, J. Monty, D. Chung, and I. Marusic, "Amplitude and frequency modulation in wall turbulence," J. Fluid Mech. **712**, 61–91 (2012).
[28]L. Agostini and M. Leschziner, "On the departure of near-wall turbulence from the quasi-steady state," J. Fluid Mech. **871**, R1 (2019).
[29]A. Altıntaş, L. Davidson, and S. Peng, "A new approximation to modulation-effect analysis based on empirical mode decomposition," Phys. Fluids **31**, 025117 (2019).
[30]N. Benard, K. D. Bayoda, A. Gaucheron, A. P. Bonnet, and E. Moreau, "In plane wavy streamwise wall forcing for turbulent skin friction drag reduction," in Aerospace Europe Conference, Bordeaux, France, 2020.
[31]L. Davidson and S. H. Peng, "Hybrid LES-RANS: A one-equation SGS model combined with a k–ω model for predicting recirculating flows," Int. J. Numer. Methods Fluids **43**, 1003–1018 (2003).
[32]P. Emvin and L. Davidson, "Development and implementation of a fast large eddy simulations method," Department of Thermo and Fluid Dynamics, Chalmers University of Technology, Gothenburg, 1997.
[33]C. M. Rhie and W. L. Chow, "Numerical study of the turbulent flow past an airfoil with trailing edge separation," AIAA J. **21**, 1525–1532 (1983).
[34]D. Elam, "A direct numerical simulation of dielectric barrier discharge (DBD) plasma actuators for turbulent skin-friction control," Ph.D. thesis, University of Warwick, 2012.
[35]D. Greenblatt, T. Schneider, and C. Y. Schüle, "Mechanism of flow separation control using plasma actuation," Phys. Fluids **24**, 077102 (2012).
[36]M. Lee and R. D. Moser, "Direct numerical simulation of turbulent channel flow up to $Re_\tau \approx 5200$," J. Fluid Mech. **774**, 395–415 (2015).
[37]H. Choi, P. Moin, and J. Kim, "Active turbulence control for drag reduction in wall-bounded flows," J. Fluid Mech. **262**, 75–110 (1994).
[38]J. C. del Álamo and J. Jiménez, "Spectra of the very large anisotropic scales in turbulent channels," Phys. Fluids **15**, L41–L44 (2003).
[39]J. M. Hamilton, J. Kim, and F. Waleffe, "Regeneration mechanisms of near-wall turbulence structures," J. Fluid Mech. **287**, 317–348 (1995).
[40]J. Kim, P. Moin, and R. Moser, "Turbulence statistics in fully developed channel flow at low Reynolds number," J. Fluid Mech. **177**, 133–166 (1987).
[41]R. D. Moser and P. Moin, "Direct numerical simulation of curved turbulent channel flow," Technical Report No. 85974, NASA, 1997.